

## Article

# Geology and Geochronology of Magmatic–Hydrothermal Breccia Pipes in the Yixingzhai Gold Deposit: Implications for Ore Genesis and Regional Exploration

Li-Zhong Zhang<sup>1,2,3</sup>, Wen-Sheng Gao<sup>1,2</sup> and Xiao-Dong Deng<sup>1,2,\*</sup>

<sup>1</sup> State Key Laboratory of Geological Processes and Mineral Resources, China University of Geosciences, Wuhan 430074, China

<sup>2</sup> School of Earth Resources, China University of Geosciences, Wuhan 430074, China

<sup>3</sup> Mineral Exploration Institute, Zijin Mining Group Co., Xiamen 361006, China

\* Correspondence: dengxiaodong@cug.edu.cn

**Abstract:** Magmatic–hydrothermal breccia pipes are widespread in numerous major porphyry and epithermal gold deposits globally, representing significant repositories of metal resources and serving as potential indicators for exploration targeting. More than ten breccia pipes occur in the Central Taihangshan District (CTD) of the North China Craton. Some of these breccia pipes host gold mineralization and are proposed to be related to the adjacent lode gold mineralization. However, the lack of detailed geological constraints make this hypothesis ambiguous. To address this, the present study conducted comprehensive field observations, drill core logging, an in situ sulfur isotope analysis of pyrite, and the <sup>40</sup>Ar/<sup>39</sup>Ar dating of adularia along a 1400 m section of the Tietangdong breccia pipe at Yixingzhai. Three distinct breccia facies were identified at Tietangdong, exhibiting variable proportions across the entire section, including a massive skarn breccia; polymictic, skarn matrix-supported breccia; and polymictic, intrusive rock cement chaotic breccia. Furthermore, adularia <sup>40</sup>Ar/<sup>39</sup>Ar dating indicates a syn-/post-gold mineralization age of 136 ± 1.5 Ma, coinciding with the age of post-breccia felsite dike. The deepest sampled pyrite displays δ<sup>34</sup>S values of ~2.7‰, strongly indicating a magmatic–hydrothermal signature. These results, when combined with the geological, geochronological, and isotopic studies on the adjacent lode gold mineralization, further suggest a close genetic relationship between the breccia pipes and the lode Au mineralization, paving the way for their utilization as effective indicators for gold targeting within the CTD.

**Keywords:** North China Craton; Central Taihangshan District; breccia pipes; gold mineralizations; sulfur isotope; adularia dating



**Citation:** Zhang, L.-Z.; Gao, W.-S.; Deng, X.-D. Geology and Geochronology of Magmatic–Hydrothermal Breccia Pipes in the Yixingzhai Gold Deposit: Implications for Ore Genesis and Regional Exploration. *Minerals* **2024**, *14*, 496. <https://doi.org/10.3390/min14050496>

Academic Editors: Galina Palyanova and Pierfranco Lattanzi

Received: 2 February 2024

Revised: 29 April 2024

Accepted: 2 May 2024

Published: 8 May 2024



**Copyright:** © 2024 by the authors. Licensee MDPI, Basel, Switzerland. This article is an open access article distributed under the terms and conditions of the Creative Commons Attribution (CC BY) license (<https://creativecommons.org/licenses/by/4.0/>).

## 1. Introduction

Porphyry and epithermal gold deposits represent a crucial and economically significant class within the spectrum of gold deposits [1,2]. Magmatic–hydrothermal breccia pipes have been reported in some giant porphyry and epithermal gold deposits [3–7], such as the Cripple Creek gold deposit, USA [8,9], Mt. Polley Cu–Ag–Au porphyry deposit, Canada [10], Kellan gold deposit, Indonesia [11], and Ladolam epithermal gold deposit, Papua New Guinea [12]. As such, the magmatic–hydrothermal breccia pipe is a potential indicator for porphyry and epithermal gold deposit exploration [13]. The magmatic–hydrothermal breccia pipe is characterized by the mechanical disruption of wall rocks resulting from the release of overpressured magmatic–hydrothermal fluids or the subsurface emplacement of intrusions [3]. In contrast, other breccia pipes, such as phreatic breccia and pebble dikes, share some similar textures with magmatic–hydrothermal breccias, but lack significant mineralization [3]. Therefore, determining the genesis of breccia pipes is crucial in evaluating the relationships between breccia pipes and mineralization.

Numerous breccia pipes have been identified in the Central Taihangshan District (CTD) within the central North China Craton (NCC) (Figure 1b, Refs. [14,15]). This district hosts numerous early Cretaceous hydrothermal ore deposits, encompassing porphyry Cu-Mo [16], skarn Fe-Au, lode Au [17,18], and volcanic-hosted Pb-Zn deposits [19]. More than ten breccia pipes have been found adjacent to these deposits, such as the Yixingzhai, Gaofan, Tanshang, Zhijiadi, and Chakou deposits (Figure 1b) [14]. It is uncertain whether these breccia pipes are associated with their adjacent hydrothermal mineralization due to poor geological constraints.

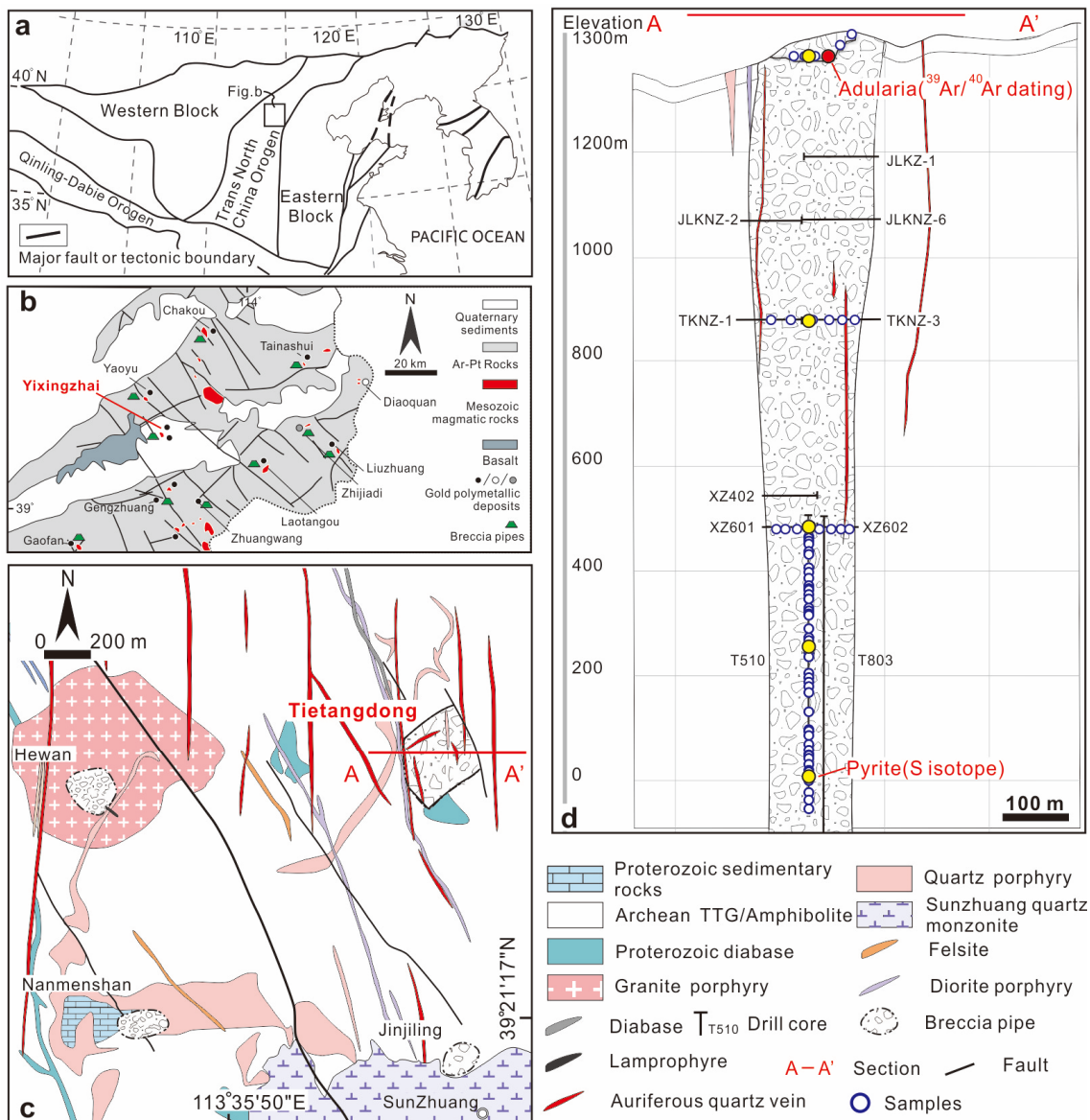


**Figure 1.** (a) Geological map showing the tectonic division of the NCC and the location of the CTD. (b) Regional geological map illustrating the distribution of the early Cretaceous magma, breccia pipes, and gold polymetallic deposits in the CTD. Geological map (c) and cross-section along the A-A' transect (d) of the Tietangdong breccia pipe (modified after [14]).

The Yixingzhai gold deposit (Lat. 39°21'51" N, Long. 113°35'46" E) is the largest gold deposit in the CTD (Figure 1c, Ref. [20]). It has sixteen lode Au ore bodies and four breccia pipes that also host gold mineralization. The Tietangdong breccia pipe is the most gold-rich breccia pipe (~20 t Au). Previous works [21–23] have suggested a skarn crypto-explosive origin for Tietangdong based on samples collected from the shallow part of the breccia pipe.

Moreover, the authors of [22] analyzed zoning textures within garnet and epidote grains, inferring several magmatic–hydrothermal pulses and multiple crypto-explosion events in Tietangdong. However, our understanding of breccia facies and their spatial distribution is still poor due to the inability to obtain deep samples, impacting insights into fully comprehending the genesis of gold mineralization within the Tietangdong breccia pipe. Furthermore, the absences of syn-gold mineralized geochronological and isotopic fluid source tracing studies limit our understanding of its relationship with the adjacent lode Au mineralization, thereby diminishing the efficacy of utilizing breccia pipes as a targeting indicator. The Zijin Mining Company recently initiated a series of drilling campaigns at the Tietangdong breccia pipe, with some drill holes reaching a depth of ~1400 m below the surface. These drilling campaigns provide an opportunity to address the issues mentioned above. The present study conducted comprehensive field observations and drill core logging across a deep cross-section (1400 m in depth), the  $^{40}\text{Ar}/^{39}\text{Ar}$  dating of syn-ore adularia, and an in situ sulfur isotope analysis of pyrite grains associated with the native gold. The results collectively provide valuable insights into the ore's genesis and regional gold exploration.

## 2. Geological Background

The CTD is located in the northern part of the ca. 1.85 Ga Trans-North China Orogen (Figure 1a, Ref. [24]). Within the CTD, the basement rocks comprise Archean to Paleoproterozoic tonalite–trondhjemite–granodiorite gneiss (TTG), amphibolite, and banded iron formation [24,25]. The NCC remained relatively stable from the late Paleoproterozoic to the Paleozoic, accumulating a substantial sequence of carbonate and clastic sediments [26]. The deep NE-trending faults in the basement, together with the NW-trending faults, constitute the primary structural framework of the CTD during the Precambrian. Subsequently, these faults experienced reactivation during the Mesozoic [14,26]. Along these faults, numerous intermediate to felsic plutons, stocks, and dikes intruded the ancient basement of the CTD (Figure 1b [27]). These felsic intrusions, with zircon U-Pb ages at 142–130 Ma [18,28,29], are interpreted as products of crust–mantle interactions resulting from the lithospheric destruction of the NCC [30]. Many porphyry Cu-Mo deposits, skarn Fe-Au deposits, and lode Au deposits formed within or around these early Cretaceous intrusions (Figure 1b). Previous molybdenite Re-Os, garnet U-Pb, titanite U-Pb, and phlogopite  $^{40}\text{Ar}/^{39}\text{Ar}$  geochronological studies revealed that the mineralization formed in the period of 140–130 Ma, concurrent with the early Cretaceous intrusions [17,18,21,30–32]. Numerous breccia pipes have been identified in the CTD [15]. These pipes are structurally controlled by the NW- and NE-trending faults and have spatial relationships with these early Cretaceous intrusions and mineralization (Figure 1b).

The Yixingzhai deposit is the largest gold deposit in the central CTD (Figure 1b). It is characterized by four breccia pipes and sixteen NW-trend auriferous quartz veins hosted in the Archean to Paleoproterozoic TTG basement. Additionally, amphibolite, metamorphic diabase, and carbonate wall rocks have been identified in the ore field (Figure 1c, Ref. [14]). Yixingzhai features multiple generations of 135–140 Ma intermediate to felsic intrusive dikes, stocks, and plutons (Figure 1c), including the Hewan granite porphyry, Nanmenshan quartz porphyry, and Sunzhuang quartz monzonite (Figures 1c and 2a–d) [17,18,20,21,30]. Four breccia pipes in the Yixingzhai gold deposit are identified along these intrusions: Tietangdong, Hewan, Nanmenshan, and Jinjiling (Figure 1c).

Sixteen lode Au ore bodies are hosted in Paleo–Proterozoic TTG gneiss and/or granite porphyry, ranging in thickness from 0.05 to 4.30 m (Figure 1c). These ore bodies extend for lengths of 150–2300 m and downdip for 500–1100 m. They exhibit a diverse mineralogical composition, including quartz, hematite, pyrite, chalcopyrite, sphalerite, and galena, with the dominant alteration characterized by sericite and chlorite [17,30].

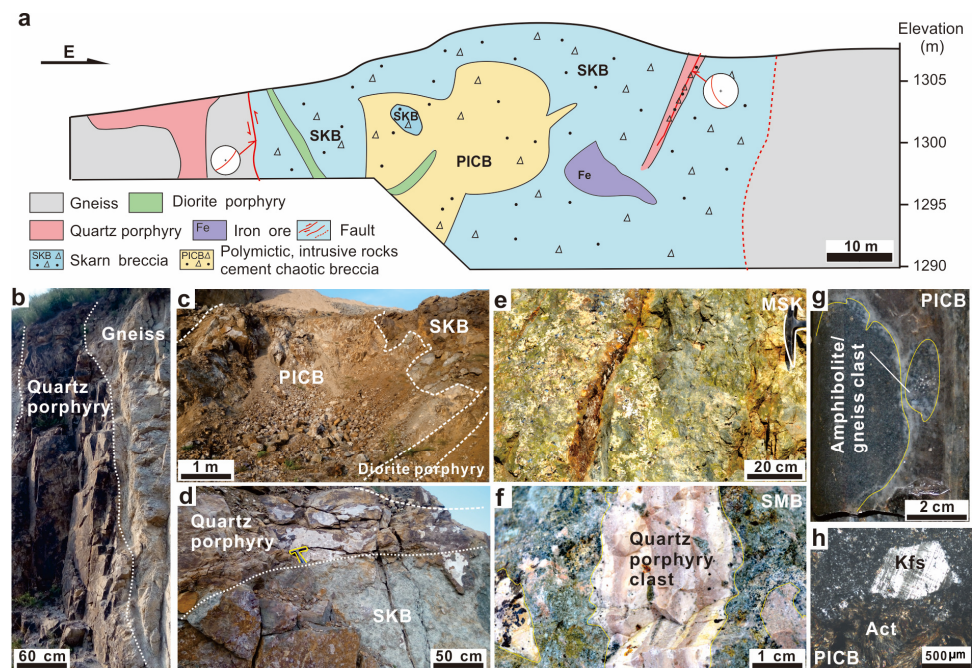


**Figure 2.** (a) Schematic cross-section showing the spatial distribution of different breccia facies, faults, and dikes in Tietangdong. Stereographic maps of faults along the margin of the Tietangdong breccia pipe are presented. (b) Quartz porphyry cutting the gneiss at the western part of the Tietangdong breccia pipe. (c) Outcrop of polymictic, intrusive rock cement chaotic breccia (PICB) and skarn breccia (SKB) in the middle of the Tietangdong breccia pipe. (d) Quartz porphyry cutting the SKB at the middle of the Tietangdong breccia pipe. (e) Massive skarn breccia (MSK) at the Tietangdong breccia pipe, displaying aggregations of massive prograde and retrograde skarn minerals with fine to medium grain sizes. Definitive contact boundaries between clasts and matrix/cement are absent. (f) Polymictic, skarn matrix-supported breccia (SMB) in the Tietangdong breccia pipe, exhibiting a matrix-supported texture. Polymictic, rounded to sub-rounded clasts include quartz porphyry, felsite, gneiss, and amphibolite. (g) PICB at the Tietangdong breccia pipe, where gray felsite (h) cements rounded gneiss and amphibolite clasts. Abbreviations: Kfs—K feldspar, Act—actinolite.

### 3. Sample and Methods

More than 300 samples, ranging from the open pit to the deep drill cores, were collected for petrographical observation and breccia facies identification (Figure 1d). The classification of breccia pipe facies follows the methodologies established in [11,12]. Specifically, the matrix comprises tiny grains of rock powder or skarn minerals that are derived from the carbonate clasts undergoing metasomatism. The cement component denotes the intrusive rocks that cement the clasts within the breccia pipe. Over 100 double-polished thin sections were examined under an optical microscope to investigate the mineralogy and textural features based on their optical properties, such as the refractive index, birefringence, interference colors, and extinction characteristics. In addition to optical microscopy, carbon-coated sections were further studied using backscattered electron (BSE) imaging with a Quanta 450 FEG scanning electron microscope (SEM) at the State Key Laboratory of Geological Processes and Mineral Resources (GPMR), China University of Geosciences (CUG). The accelerating voltage was set to 15 kV, with a beam current of 20 nA. The SEM-BSE technique provided valuable information about the elemental contrast and micro-textural relationships, which are crucial for identifying minerals with similar optical properties. In cases where further confirmation was necessary, energy-dispersive X-ray spectroscopy (EDS) was employed to analyze the chemical composition of the minerals, ensuring accurate identification. Detailed sample descriptions and logging results are listed in Supplementary Material S1 (Table S1) and illustrated in Figure 3.

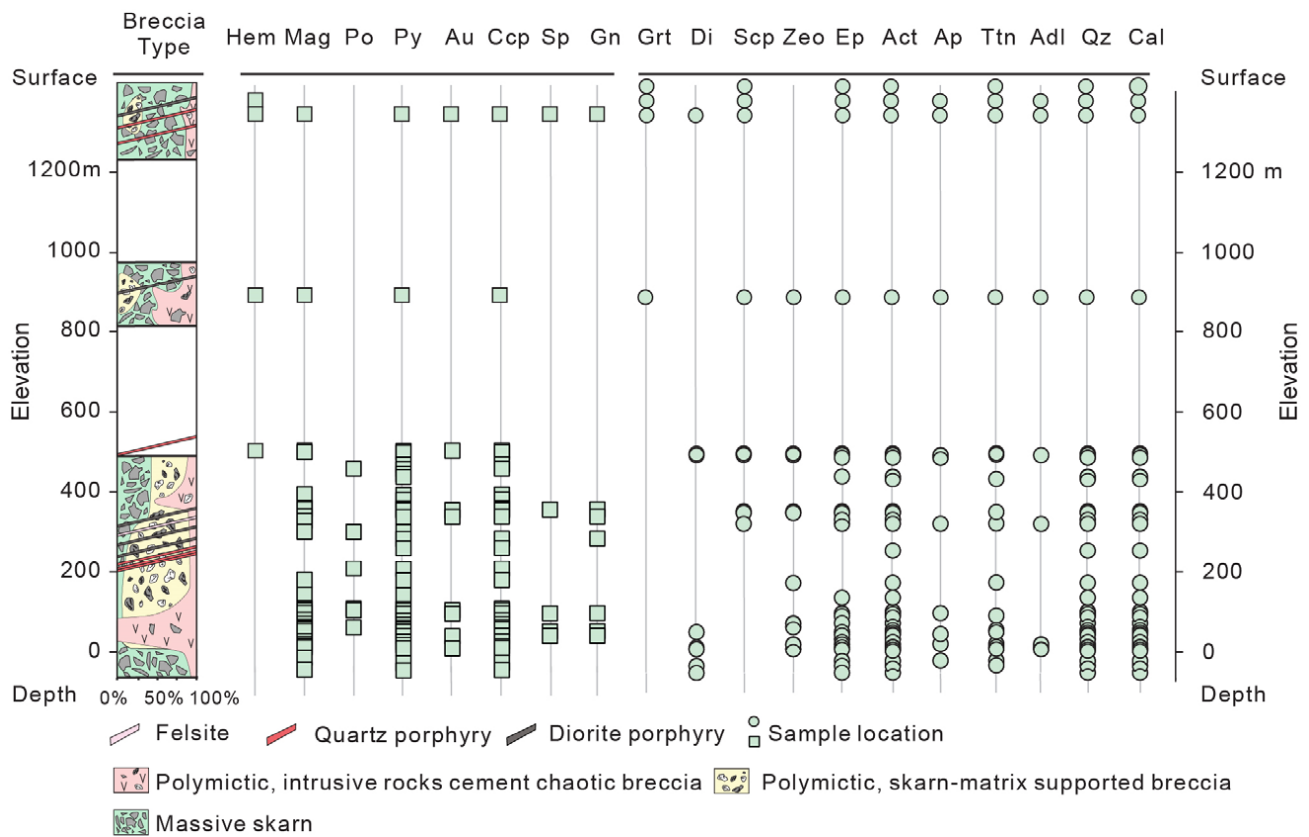


**Figure 3.** Cross-sectional illustration depicting breccia facies, intrusive rocks, and mineral associations in the Tietangdong breccia pipe. Abbreviations: Hem—hematite, Mag—magnetite, Po—pyrrhotite, Py—pyrite, Au—native gold, Ccp—chalcopyrite, Sp—sphalerite, Gn—galena, Grt—garnet, Di—diopside, Scp—scapolite, Zeo—zeolite, Ep—epidote, Act—actinolite, Ap—apatite, Ttn—titanite, Adl—adularia, Qz—quartz, Cal—calcite.

### 3.1. Adularia $^{40}\text{Ar}/^{39}\text{Ar}$ Dating

The sample TTD-10 was collected from the open pit for adularia  $^{40}\text{Ar}/^{39}\text{Ar}$  dating, with adularia and calcite cementing the retrograde epidote and actinolite (Figure 4c). After careful petrographic observation, adularia was extracted through a series of steps: crushing, sieving, washing in distilled water using an ultrasonic bath for 10 min, and air-drying for two days. Finally, 0.5 to 2.0 mm adularia grains were handpicked under a binocular microscope and validated via SEM-EDS before  $^{40}\text{Ar}/^{39}\text{Ar}$  dating.

The mineral separates were irradiated with ZBH-2506 biotite standards ( $132.7 \pm 0.2$  Ma [33]) in the China Mianyang Research Reactor (CMRR) at the China Academy of Engineering for 48 h. After cooling for three months, the argon isotope ratios were analyzed using the incremental heating method on a multi-collector Argus VI noble gas mass spectrometer connected to a Coherent 50W  $\text{CO}_2$ -IR laser device at the  $^{40}\text{Ar}/^{39}\text{Ar}$  laboratory at CUG. The experimental details of the method were provided in [34]. The  $^{40}\text{Ar}/^{39}\text{Ar}$  results were calculated and plotted using the ArArCALC (version 2.52b [35]) software. All dates were reported using  $5.543 \times 10^{-10} \text{ a}^{-1}$  as the total decay constant for  $^{40}\text{K}$  [36], with reactor correction factors set at  $8.984 \times 10^{-4}$  for  $(^{39}\text{Ar}/^{37}\text{Ar})_{\text{Ca}}$ ,  $2.673 \times 10^{-4}$  for  $(^{36}\text{Ar}/^{37}\text{Ar})_{\text{Ca}}$ , and  $5.97 \times 10^{-3}$  for  $(^{40}\text{Ar}/^{39}\text{Ar})_{\text{K}}$ .

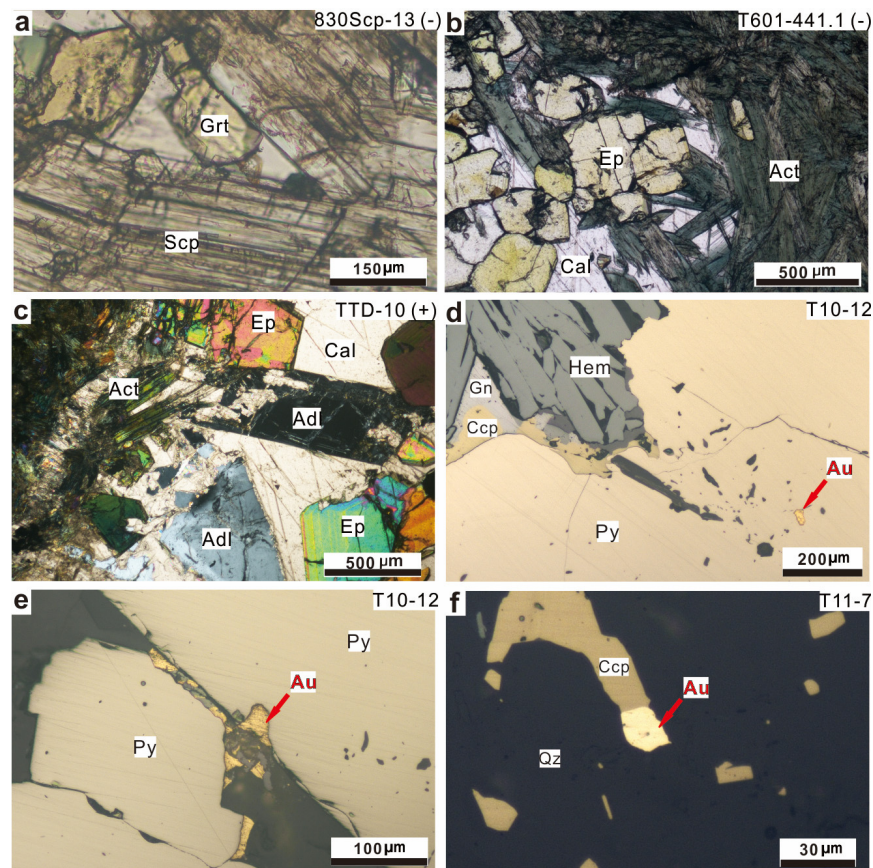


**Figure 4.** Microphotographs illustrating mineral associations and the occurrences of gold grains at the Tietangdong breccia pipe. (a) Garnet coexists with scapolite during the prograde skarn stage. (b) Epidote coexists with actinolite during the retrograde skarn stage, cemented by late-stage calcite. (c) Calcite and adularia at the quartz–sulfide–calcite stage cement the early stage epidote and actinolite. Microphotographs show anhedronal native gold either as inclusions (d) or filling the interstitial of pyrite and chalcopyrite (e,f) at the Tietangdong breccia pipe. Abbreviations: Au—native gold, Hem—hematite, Py—pyrite, Ccp—chalcopyrite, Sp—sphalerite, Gn—galena, Grt—garnet, Scp—scapolite, Ep—epidote, Act—actinolite, Qz—quartz, Cal—calcite, Adl—adularia, ‘+’ —under cross-polarized light, ‘-’ —under plane-polarized light.

### 3.2. In Situ Sulfur Isotope Analysis

Five samples from the Tietangdong breccia pipe were selected for in situ sulfur isotope analysis. In situ sulfur isotope analyses of pyrite that related to gold inclusions were carried out using an NWR Femto<sup>UC</sup> femtosecond system (New Wave Research, Fremont, CA, USA) coupled with a Neptune Plus multi-collector inductively coupled plasma mass spectrometer (MC-ICPMS, Thermo Fisher Scientific, Bremen, Germany) at the GPMR, CUG. In the laser ablation system, helium was used as the carrier gas for the ablation cell and was mixed with argon (make-up gas) after the ablation cell. Single-spot ablation mode was employed. The laser fluence was kept constant at  $\sim 2.5 \text{ J/cm}^2$ . To mitigate the downhole fractionation effect, a large spot size (40  $\mu\text{m}$ ) and slow pulse frequency (4 Hz) were utilized [37]. The Neptune Plus, equipped with nine Faraday cups fitted with  $10^{11} \Omega$  resistors, collected isotopes  $^{32}\text{S}$ ,  $^{33}\text{S}$ , and  $^{34}\text{S}$  in static mode. The X skimmer cone and Jet sample cone in Neptune Plus were used to improve the signal intensity. Nitrogen (4 mL/min) was introduced into the central gas flow to diminish the polyatomic interferences. Medium resolution was applied in all measurements, with the revolving power kept at greater than 5000.

The standard-sample bracketing method (SSB) was employed to correct instrumental mass fractionation. The external standard of pyrite PPP-1 ( $\delta^{34}\text{S} = 5.40\text{‰} \pm 0.16\text{‰}$ ) was used to correct the mass fractionation of the sulfur isotope in various sulfide samples. In

addition, the in-house references of pyrrhotite YP136 ( $\delta^{34}\text{S} = 1.50\text{‰} \pm 0.30\text{‰}$  [38]) were repeatedly analyzed to verify the calibration accuracy. The analyzed  $\delta^{34}\text{S}$  results of YP136 were  $1.44\text{‰} \pm 0.18\text{‰}$  ( $n = 10, 2\sigma$ ). All data reductions for the LA-MC-ICPMS analysis were conducted using the ISO-Compass software [39].

## 4. Results

### 4.1. Breccia Facies and Intrusive Sequences

Based on the clasts composition, matrix characteristics, and cement types [11,12], the breccia facies of the Tietangdong breccia pipe can be classified into two main facies: the skarn breccia (SKB) and the polymictic intrusive rock cement-supported chaotic breccia (PICB) (Table 1).

**Table 1.** Classification of breccia facies in the Tietangdong breccia pipe.

Breccia Facies	Interpretation	Component				Internal Organization and Mineralization	Spatial Distribution	
		Clast	Matrix	Cement	Open Space			
Massive skarn (MSK)	Magmatic–hydrothermal breccia	Aggregates of massive prograde and retrograde skarn minerals (Grt, Scp, Di, Act, Ep, Qz, Chl, and Cal) with fine to medium grain sizes (2–64 mm), commonly lacking definitive boundaries between the clasts and the cement; ore minerals include Mag, Hem, Py, Ccp, Sp, Gn, and Au			<5 vol.% vugs	Massive skarn ores, mainly bearing low to high grades of gold and iron		
Skarn breccia (SKB)	Polymictic, skarn matrix-supported breccia (SMB)	Magmatic–hydrothermal breccia	5–70 vol.%; generally rounded to sub-rounded; polymictic clasts, including felsite, gneiss, amphibolite, and a few skarn carbonate clasts; the clasts measure 5–30 mm, with blocks measuring up to 20 cm occasionally	30–95 vol.%; skarn minerals (Scp, Act, Ep, Py, Ccp) that are predominantly 1–2 mm	–	<5 vol.% vugs	Chaotic; mainly matrix supported; no high grade of gold	Mainly distributed at the top of the Tietangdong breccia pipe
Polymictic, intrusive rock cement chaotic breccia (PICB)	Intrusive breccia		10–75 vol.%; rounded to sub-rounded; polymictic clasts, including partly skarn carbonate clasts, gneiss, amphibolite, and some felsite clasts; the clasts measure 5–60 mm	–	15–90 vol.%; igneous rocks (felsite, granite porphyry, and diorite porphyry)	–	Chaotic; cement supported to clast supported; rarely mineralized	Mainly distributed at the bottom of the Tietangdong breccia pipe

The SKB can be categorized as a massive skarn breccia (MSK) and a polymictic skarn matrix-supported breccia (SMB). The MSK is characterized by aggregates of massive prograde and retrograde skarn minerals, including garnet, scapolite, diopside, actinolite, epidote, quartz, chlorite, and calcite (Table 1), with a grain size of 2–64 mm (Figure 4a,b). It has indistinct boundaries between the clasts and the cement (Figure 2e). Ore minerals in the MSK consist of magnetite, hematite, and pyrite (Figure 3). The MSK is widely distributed at the top of the Tietangdong breccia pipe (Figures 2a and 3). The SMB comprises polymictic clasts and a skarn matrix (Figure 2f, Table 1). Polymictic clasts comprise felsite, gneiss, amphibolite, and partly skarn carbonate clasts. Individual clasts are generally rounded to sub-rounded, measuring 5–30 mm, with blocks up to 20 cm occasionally. The matrix is mainly composed of skarn minerals, including scapolite, actinolite, epidote, and some sulfide minerals (pyrite and chalcopyrite), predominately in the size of 1–2 mm (Figure 2f). The SMB is primarily distributed at the top of the Tietangdong breccia pipe (Figures 2a and 3).

The PICB (Figure 2c,g, Table 1) exhibits chaotic characteristics and transitions from cement-supported to clast-supported. Polymictic clasts encompass partly skarn carbonate, gneiss, amphibolite, and some felsite clasts (Figure 2g). These individual clasts generally display rounded to sub-rounded shapes, with sizes ranging from 5 to 60 mm (Figure 2g).

The cement mainly consists of fine-grained intrusive rocks (Figure 2g,h). The PICB is mainly distributed at the base of the Tietangdong breccia pipe (Figure 3).

Three generations of intrusive dikes have been identified through field relationships (Figure 3). The first pre-breccia stage is represented by intrusive rock fragments of the clasts, such as the felsite clasts in the SMB (Figure 2f). The second syn-breccia stage is characterized by the felsic intrusive cement in the PICB (Figure 2g). The third post-breccia stage is represented by intrusive dikes that cut the Tietangdong breccia pipe (Figures 2d and 3).

4.2. Mineralization of and Alteration in Tietangdong Breccia Pipe

The Tietangdong breccia pipe exhibits three hydrothermal alteration and mineralization stages: the prograde skarn stage, retrograde skarn stage, and quartz–sulfide–calcite stage. The prograde skarn stage consists of garnet, diopside, scapolite, and minor magnetite (Figures 3 and 4a). It is primarily concentrated in the shallow part of the breccia pipe (Figure 3, 800–1300 m above sea level). The retrograde skarn stage is characterized by scapolite, epidote, actinolite, magnetite, and minor sulfide minerals, with minor native gold (Figures 3 and 4b). It is distributed throughout the breccia pipe, often replacing or cementing the prograde skarn minerals. The quartz–sulfide–calcite stage is represented by pervasive quartz, sulfides, calcite, and adularia (Figures 3 and 4c–f). This stage is identified as the dominant gold mineralization stage. Native gold is mainly present as inclusions (5–35 μm) or filling the intergranular space of the texturally homogeneous pyrite and chalcopyrite of this stage (Figure 4d–f), with tiny irregular native Au grains (1–5 μm) sporadically adjacent along the margin of hematite, quartz, calcite, and chlorite grains [22]. The quartz–sulfide–calcite stage is distributed throughout the Tietangdong breccia pipe (Figure 3). The mineral paragenesis of the Tietangdong breccia pipe is summarized in Figure 5. In comparison to previous works [22,23], scapolite and adularia were first identified in this study. Although molybdenite was reported in an earlier work [22], we did not observe this mineral in this study (Figure 5).

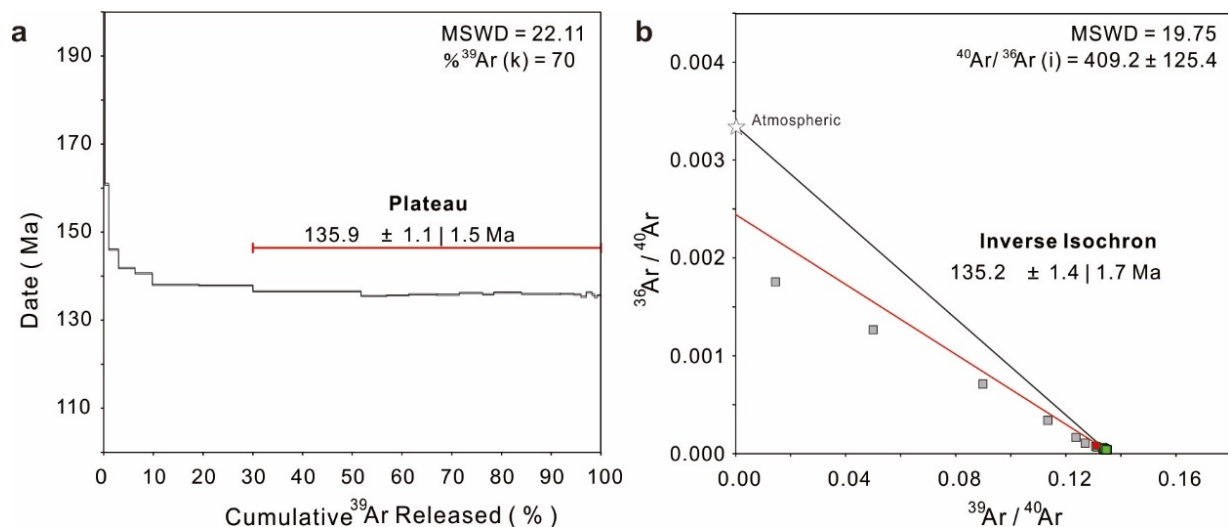
Stages Minerals	Skarn stage		Quartz–sulfide–calcite stage
	Prograde	Retrograde	
Garnet	██████████		
Diopside	██████████		
Scapolite	██████████	██████████	
Epidote		██████████	
Actinolite		██████████	
Chlorite		██████████	
Quartz		██████████	██████████
Calcite		██████████	██████████
Magnetite		██████████	
Hematite		██████████	
Pyrite		██████████	██████████
Native gold			██████████
Chalcopyrite			██████████
Bornite			██████████
Galena			██████████
Sphalerite			██████████
Tetrahedrite			██████████
Sericite			██████████
Adularia			██████████
Ankerite			██████████

Figure 5. Mineral paragenesis in the Tietangdong breccia pipe.

The breccia facies, intrusive sequences, and mineral associations along the section in the Tietangdong breccia pipe are illustrated in Figure 3. The results show that the proportions of MSK and SMB decrease with depth. However, the PICB increases with the depth in the Tietangdong breccia pipe (Figure 3). In addition, Figure 3 reveals a vertical zonation of sulfide and oxide mineral associations along the 1400 m section. This zonation encompasses two segments: (1) hematite and magnetite-bearing breccia above approximately 510 m above sea level and (2) magnetite, pyrrhotite, and pyrite-bearing breccia below 510 m above sea level (Figure 3).

#### 4.3. $^{40}\text{Ar}/^{39}\text{Ar}$ Dating of Adularia

The  $^{40}\text{Ar}/^{39}\text{Ar}$  dating results obtained for the adularia grains in sample TTD10 are illustrated as the  $^{40}\text{Ar}/^{39}\text{Ar}$  spectrum and inverse isochron plots in Figure 6, with detailed data in Supplementary Material S2 (Table S2). The adularia  $^{40}\text{Ar}/^{39}\text{Ar}$  spectra show anomalously old apparent ages at low-temperature steps, followed by several continuous plateau ages ( $135.9 \pm 1.5$  Ma,  $2\sigma$  level, full external uncertainty considering the decay constant,  $\Sigma^{39}\text{Ar} = 70\%$ ) at mid-high temperature steps (Figure 6a). The old apparent ages at low-temperature steps are interpreted as  $^{39}\text{Ar}$  loss in intercrystallite and/or damaged sites of adularia through recoil during irradiation [40]. Then, argon in the tight crystallographic reservoir of adularia releases at mid-high temperature steps and forms the plateau age (Figure 6a), which can be interpreted as the timing of adularia formation. In addition, the adularia grains also yield an isochron age of  $135.2 \pm 1.7$  Ma (Figure 6b), which is consistent with its plateau age. This consistency supports the adularia formed at ca. 136 Ma in the Tietangdong breccia pipe.



**Figure 6.** Laser-heated  $^{40}\text{Ar}/^{39}\text{Ar}$  date spectra (a) and inverse isochron (b) of adularia from the Tietangdong breccia pipe.

#### 4.4. In Situ Sulfur Isotopes of Pyrite

Sixteen spot analyses of pyrite from the Tietangdong breccia pipe yielded  $\delta^{34}\text{S}$  values ranging from 2.03‰ to 9.01‰, with a mean of 4.08‰ (Figure 7a; Table 2). These results strongly illustrate decreased pyrite  $\delta^{34}\text{S}$  values with increasing depth within the Tietangdong breccia pipe (Figure 7b). Specifically, at elevations of 15 m, 258 m, 510 m, 830 m, and 1380 m, the  $\delta^{34}\text{S}$  values exhibit ranges of 2.48‰–2.73‰, 2.03‰–2.63‰, 2.10‰–4.22‰, 3.98‰–9.01‰, and 5.29‰–6.59‰, respectively.

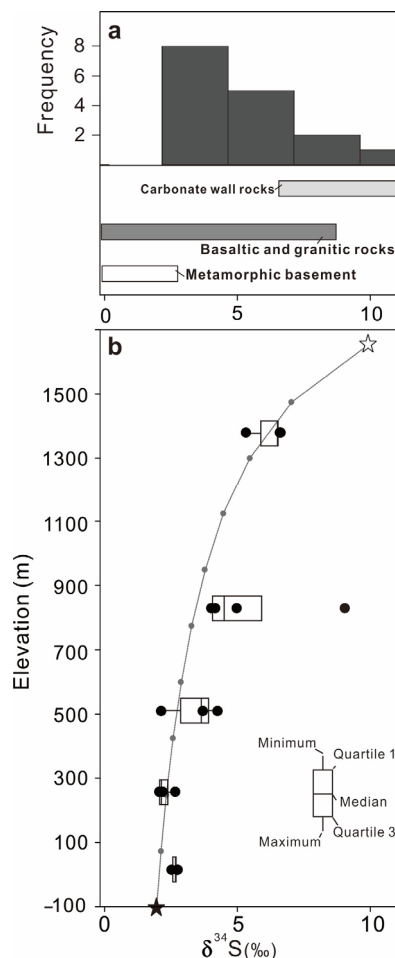


**Figure 7.** (a) Comparison of sulfur isotope results from the Tietangdong breccia pipe. The boxes represent the reported isotopic ranges of sulfur isotope values from different reservoirs [26,41,42]. (b) Depth profile of pyrite sulfur isotope from the Tietangdong breccia pipe. The linear regression curve illustrates a two-end member mixing trend between the magmatic–hydrothermal fluids (assuming 2‰ of  $\delta^{34}\text{S}$  and 1000 ppm of sulfur contents at an elevation of –100 m) and the ore field carbonate wall rocks (assuming 10‰ of  $\delta^{34}\text{S}$  and 200 ppm of sulfur contents at an elevation of 1450 m).

**Table 2.** The sulfur isotope analysis results in the Tietangdong breccia pipe.

Sample no.	Elevation (m)	Minerals	$\delta^{34}\text{S}$ (‰)	2SD (‰)	Secondary Standard	$\delta^{34}\text{S}$ (‰)	2SD (‰)
T601-494.7-01	15	Pyrite	2.48	0.10	YP136	1.33	0.12
T601-494.7-02	15	Pyrite	2.69	0.10	YP136	1.56	0.16
T601-494.7-03	15	Pyrite	2.73	0.11	YP136	1.44	0.16
T601-251.6-01	258	Pyrite	2.63	0.10	YP136	1.49	0.09
T601-251.6-02	258	Pyrite	2.03	0.10	YP136	1.51	0.11
T601-251.6-03	258	Pyrite	2.16	0.08	YP136	1.39	0.18
T11-16-2-01	1380	Pyrite	6.59	0.11	YP136	1.27	0.12
T11-16-2-02	1380	Pyrite	6.56	0.11	YP136	1.49	0.15
T11-16-2-03	1380	Pyrite	5.29	0.11	YP136	1.41	0.14
830-9-01	830	Pyrite	3.98	0.13	YP136	1.55	0.12
830-9-02	830	Pyrite	4.13	0.12			
830-9-03	830	Pyrite	9.01	0.14			
830-9-04	830	Pyrite	4.94	0.16			
T510-3-2-01	510	Pyrite	3.67	0.10			
T510-3-2-02	510	Pyrite	4.22	0.11			
T510-3-2-03	510	Pyrite	2.10	0.10			

## 5. Discussion

### 5.1. Discrimination and Genesis of Breccia Facies

Detailed field observation and drill core logging identified three breccia facies at Tietangdong, including massive skarn breccia (MSK), polymictic, skarn matrix-supported breccia (SMB), and polymictic, intrusive rock cement chaotic breccia (PICB) (Figure 3). The presence of high-salinity fluid inclusions in skarn minerals [31] in the MSK and SMB suggests a magmatic–hydrothermal origin of the Tietangdong breccia pipe [43]. The identification of PICB further substantiates this conclusion. The PICB exhibits felsite as cement for both wall rock and skarn clasts, providing evidence of the direct involvement of intrusive rocks in the formation of the Tietangdong breccia pipe. Moreover, the increasing prevalence of PICB in deeper segments of the breccia pipe (Figure 3) indicates heightened intrusive activities. The widespread occurrence of felsite and diorite clasts in PICB and SMB, along with post-breccia felsite and diorite dikes (Figures 2–4), suggests significant intrusive processes both preceding and succeeding the breccia pipe formation. In summary, our comprehensive geological observations across the 1400 m section confirm the magmatic–hydrothermal origin of the Tietangdong breccia pipe.

### 5.2. The Age of Breccia-Hosted Au Mineralization at Tietangdong

Adularia is prevalent at the quartz–sulfide–calcite stage (Figure 4c). Given the lower temperature of adularia crystallization [44], in line with the low closure temperature of the  $^{40}\text{Ar}/^{39}\text{Ar}$  system [45], adularia is a promising candidate for constraining the time of syn-/post-gold mineralization at Tietangdong. Consequently, the obtained date of  $135.9 \pm 1.5$  Ma (Figure 6) may represent the age of gold mineralization in the Tietangdong breccia pipe. Although this age coincides well with the pre-gold garnet U-Pb dating result of  $139 \pm 4$  Ma [21], it exhibits a slight inconsistency with the zircon U-Pb age of the post-breccia quartz porphyry ( $141 \pm 1$  Ma, ref. [21]). This discrepancy might be derived from the application of different radiometric dating systems and analytical methods. After accounting for their systematic and the decay constant uncertainties of  $^{40}\text{Ar}/^{39}\text{Ar}$  (~2%, total relative uncertainty [45–47]) and U-Pb (~3%, total relative uncertainty [45–47]), the overlapping results around ca. 136 Ma are revealed. In summary, the spatial and temporal evidence strongly support a close genetic relationship between gold mineralization and the intrusive rocks at the Tietangdong breccia pipe. Furthermore, the age of Tietangdong gold mineralization is consistent with the zircon U-Pb age of the syn-/post-lode Au Sunzhuang pluton (ca. 135 Ma, refs. [18,30]), indicating a potential genetic relationship between the breccia-hosted gold mineralization and lode Au mineralization. The sulfur isotope results below provide additional support for this hypothesis.

### 5.3. The Source of Breccia-Hosted Au Mineralization at Tietangdong

Pyrite is one of the most predominant sulfide minerals, enclosing gold grains (Figure 4) within the Tietangdong breccia. Furthermore, no sulfate has been identified in the whole section. Consequently, the sulfur isotopes of pyrite could be a reliable proxy for the sulfur isotope of hydrothermal fluids at Tietangdong [48]. The sulfur isotopes of the pyrite from the Tietangdong breccia pipe exhibit a variation of 2.03‰–9.01‰ (Figure 7a). Despite aligning with the sulfur range of the regional metamorphic basement ( $\delta^{34}\text{S}$  values of –10.0‰ to 2.0‰, ref. [26]), the absence of an early Cretaceous metamorphic event in the CTD precludes the involvement of metamorphic fluids [49]. In addition, the identification of daughter crystal-bearing fluid inclusions in garnet grains [21] indicates high-salinity ore-forming fluids, distinguishing them from the typical low-salinity and  $\text{CO}_2$ -rich fluid inclusions associated with metamorphic hydrothermal fluids [50].

Most sulfur isotopes fall within the global magmatic–hydrothermal fluids range ( $\delta^{34}\text{S}$  values of –1‰ to 8‰, ref. [41], Figure 7), implying a magmatic–hydrothermal origin of the ore-forming fluid. Furthermore, the  $\delta^{34}\text{S}$  values exhibit a positive elevation-related fractionation trend within the Tietangdong breccia pipe (Figure 7). This trend could be explained using a scenario involving gradually diminishing water–rock interactions be-

tween exsolved magmatic–hydrothermal fluids ( $\delta^{34}\text{S}$  values  $\sim 2\text{‰}$ ) and the carbonate wall rocks ( $\delta^{34}\text{S}$  values  $\sim 10\text{‰}$ ) [42] with the increasing depth of the breccia pipe. As Figure 3 illustrates, the decreasing proportion of skarn breccia implies a reduced involvement of carbonate wall rocks at greater depths. This shift would supply a less heavy sulfur isotope for the deep hydrothermal system than the shallow part. Therefore, lighter sulfur isotope values are revealed at depth, while heavier sulfur isotope values are retained in shallow areas. Under this assumption, a simple two-end member mixed model was employed, as depicted in Figure 7b. The simulated model aligns well with our sulfur isotope results. This alignment suggests a more pronounced magmatic–hydrothermal signature in the deeper part of the Tietangdong breccia pipe. It further implies promising potential for gold mineralization in the deep section. This view has been supported by the subsequent drill campaigns conducted by Zijin Mining Company.

An alternative interpretation of the sulfur isotope fractionation observed in this study could be linked to the redox state of hydrothermal fluids. In hydrothermal systems, an oxidized state promotes the formation of  $\text{SO}_4^{2-}$  ligands, which preferentially incorporate the heavy sulfur isotope, resulting in the depletion of the heavy sulfur isotope in pyrite [48,51,52]. However, our geological observations present a contradiction to this theoretical expectation. The presence of hematite in the shallow part and pyrrhotite in the deeper sections (Figure 3) suggests a theoretically lighter sulfur isotope composition in the shallow region and a heavier one at the base. This contradiction excludes the redox hypothesis.

The sulfur isotope composition of the deep section of the Tietangdong breccia pipe (ca.  $2.7\text{‰}$ , Table 2) closely resembles the sulfur isotope composition of the lode Au ( $0.7\text{‰}$ – $3.2\text{‰}$ , Ref. [30]). The gold mineralization age at Tietangdong breccia pipe shares a similar mineralization age with the lode Au in the Yixingzhai deposit. Moreover, both the breccia-hosted Au and lode Au orebodies are controlled by the ore-field NW-/NE-trending faults [14]. Therefore, we propose that the Tietangdong breccia pipe and the lode Au are part of the same magmatic–hydrothermal mineralization system.

#### 5.4. Genetic Model and Exploration Implications

Based on field investigations, geochronology, and sulfur isotope analysis, we propose a genetic evolution model for the Tietangdong breccia pipe and the lode Au mineralization in Yixingzhai. During the Mesozoic, NW-/NE-trending faults in Yixingzhai became active, establishing connections with deep magma reservoirs. These activities facilitated the intrusion of felsite and diorite dikes and the formation of hydrothermal conduits at ca. 135–140 Ma (Figure 8a). Along these conduits, the magmatic–hydrothermal fluids, exsolved from the deep magma reservoirs through second boiling [4], were trapped in the shallow part due to the low permeability of superficial TTG and carbonate wall rocks. Subsequently, the conjunction between the faults and the dikes, identified as structural weak points in the ore field, lost stability due to the higher pressure of the accumulated volatiles compared to the resistance of the wall rocks. This process led to a series of fault displacements, wall rock ruptures, skarn alterations, and gold mineralization. Concurrently, the continued intrusion of felsic dikes contributed to the formation of intrusive breccia in the deeper sections of the breccia pipe (Figure 8a–b). These breccia and intrusive processes could have happened several times, as revealed through the geochemistry of the distinct zonation of garnet and epidote grains [22]. Simultaneously, lode Au mineralization occurred at the Yixingzhai TTG adjacent to the Tietangdong breccia, which hosted Au mineralization. Ultimately, the Tietangdong breccia pipe was intersected by late-stage quartz and diorite dikes, followed by subsequent erosion (Figure 8c). These late-stage quartz and diorite dikes are relatively fresh and lack gold mineralization (Figures 2d and 3), contrasting with previous observations [22].

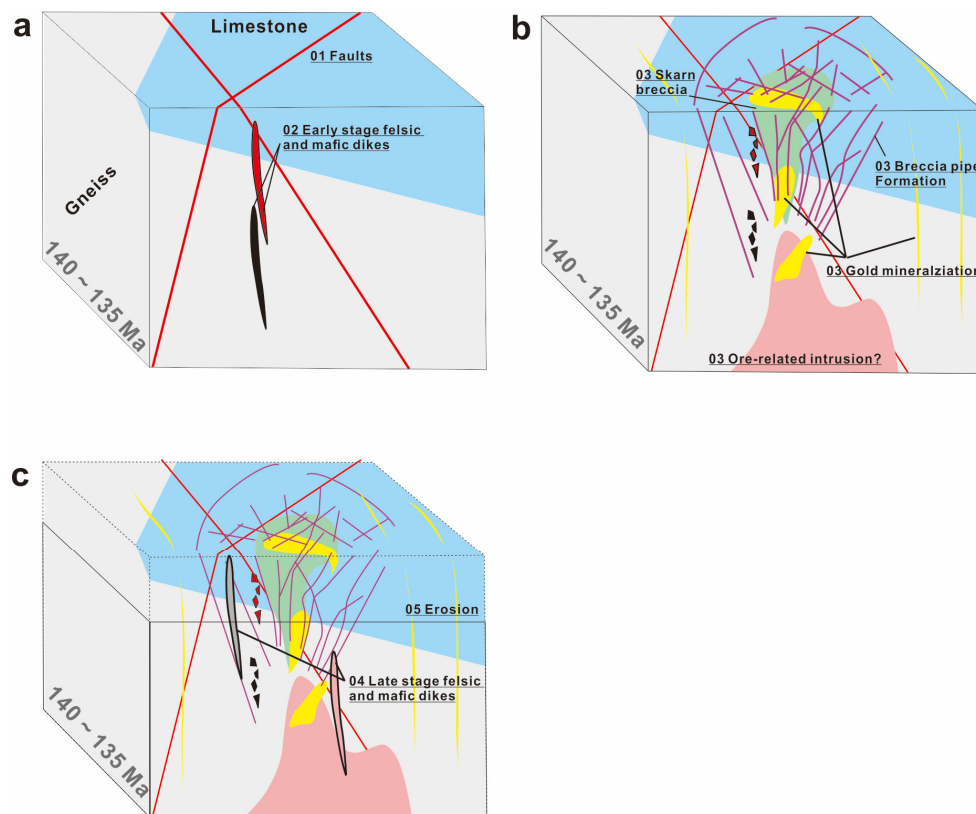


**Figure 8.** Schematic representations of the formation of Tietangdong breccia pipes (modified after [22]). (a) Pre-mineralization intrusion events. (b) Breccia pipe formation and gold mineralization processes. (c) Post-mineralization intrusion and erosion events.

This study provides valuable insights for exploration within the CTD. Firstly, this study reveals the dominance of magmatic–hydrothermal fluids in the formation of the breccia pipe, as evidenced by the abundance of intrusive rock clasts, pre-/syn-/post-breccia intrusions (Figures 2 and 3), adularia age, and sulfur isotope results (Figure 7). Additionally, a strong genetic relationship between the Tietangdong breccia pipe and gold mineralization was demonstrated in this study. This correlation suggests that breccia pipes could be a good indicator for gold targeting within the CTD. The intersections of regional NW- and NE-trending faults (Figure 1c) favor the formation of breccia pipes, which, in turn, may contribute to targeting new gold deposits, highlighting substantial exploration potential for gold in this region.

## 6. Conclusions

The present study synthesizes detailed field observations, the adularia  $^{40}\text{Ar}/^{39}\text{Ar}$  dating of  $135.9 \pm 1.5$  Ma, and a pyrite sulfur isotope analysis of  $2.03\text{‰}$ – $9.01\text{‰}$ , conclusively establishing a comprehensive geological formation model of the Tietangdong breccia pipe. Detailed field observations and drill core logging results categorize the breccia into massive skarn breccia (MSK); polymictic, skarn matrix-supported breccia (SMB); and polymictic, intrusive rock cement chaotic breccia (PICB). Furthermore, the sources and age of the Tietangdong breccia pipe align closely with those of the lode Au mineralization at the Yixingzhai deposit, indicating their potential genetic links. Numerous breccia pipes have been identified in the CTD, exhibiting geological characteristics akin to those of the Tietangdong breccia pipe and representing high potential for future gold targeting. The proposed integrated approach underscores the significance of geological, geochronological, and isotopic evidence in understanding ore genesis and informing regional gold exploration strategies.

**Supplementary Materials:** The following supporting information can be downloaded at <https://www.mdpi.com/article/10.3390/min14050496/s1>: Table S1: Breccia facies logging results of the Tietangdong breccia pipe; Table S2: Ar-Ar geochronology of adularia from the Tietangdong breccia pipe.

**Author Contributions:** Conceptualization, L.-Z.Z. and W.-S.G.; methodology, L.-Z.Z. and W.-S.G.; writing—original draft preparation, L.-Z.Z.; writing—review and editing, X.-D.D. and W.-S.G.; supervision, X.-D.D.; funding acquisition, X.-D.D. All authors have read and agreed to the published version of the manuscript.

**Funding:** This work was supported by the MOST Special Fund from the GPMR (Grant No. MSFGPMR2022-5), China University of Geosciences (Wuhan) and Zijin Mining Co. (Grant No. 2021026037). Wensheng Gao is financially supported by the China Scholarship Council (Grant No. 202106410102).

**Data Availability Statement:** All data, models, or codes that support the findings of this study are available from the corresponding author upon reasonable request.

**Acknowledgments:** We thank the Academic Editor for handling the manuscript and providing insightful comments, as well as four anonymous reviewers for their constructive feedback, which greatly improved the manuscript. Xiao-Rui Deng, Yu-Xiang Li, and Yang Yang are thanked for their help during the fieldwork and laboratory analysis. Jian-Pei Lu is thanked for the excellent sample preparation.

**Conflicts of Interest:** Zhang Li-Zhong is employed by Zijin Mining Co. Deng Xiao-Dong has received research grants from Zijin Mining Co. However, the funding sponsors played no role in the design of the study; in the collection, analysis, or interpretation of data; in the writing of the manuscript; or in the decision to publish the results.

## References

1. Frimmel, H.E. Earth's Continental Crustal Gold Endowment. *Earth Planet. Sci. Lett.* **2008**, *267*, 45–55. [[CrossRef](#)]
2. Ulrich, T.; Günther, D.; Heinrich, C.A. Gold Concentrations of Magmatic Brines and the Metal Budget of Porphyry Copper Deposits. *Nature* **1999**, *399*, 676–679. [[CrossRef](#)]
3. Sillitoe, R.H. Porphyry Copper Systems. *Econ. Geol.* **2010**, *105*, 3–41. [[CrossRef](#)]
4. Sillitoe, R.H. Ore-Related Breccias in Volcanoplutonic Arcs. *Econ. Geol.* **1985**, *80*, 1467–1514. [[CrossRef](#)]
5. Chen, J.; Cooke, D.R.; Piquer, J.; Selley, D.; Zhang, L.; White, N.C. Hydrothermal Alteration, Mineralization, and Structural Geology of the Zijinshan High-Sulfidation Au-Cu Deposit, Fujian Province, Southeast China. *Econ. Geol.* **2019**, *114*, 639–666. [[CrossRef](#)]
6. Wang, B.; Zhou, T.-F.; Fan, Y.; Chen, J.; Liu, Y.-N.; Chen, Y. Breccia, Hydrothermal Alteration and Structural Geology of the Huangtun Porphyry Au-Cu Deposit in the Middle-Lower Yangtze Metallogenic Belt, Eastern China. *Ore Geol. Rev.* **2020**, *120*, 103414. [[CrossRef](#)]
7. Sun, Y.; Wang, X.; Zhang, Y.; Li, D.; Shan, W.; Geng, K.; Wei, P.; Liu, Q.; Xie, W.; Chi, N. Cu and S Isotopes of the Main Sulfides and Indicative Significance in the Qibaoshan Cu-Au Polymetallic Ore District, Wulian County, Shandong Province, North China Craton. *Minerals* **2023**, *13*, 723. [[CrossRef](#)]
8. Jensen, E.P. Magmatic and Hydrothermal Evolution of the Cripple Creek Gold Deposit, Colorado, and Comparisons with Regional and Global Magmatic-Hydrothermal Systems Associated with Alkaline Magmatism. Ph.D. Thesis, University of Arizona, Tucson, AZ, USA, 2003.
9. Thompson, T.B.; Trippel, A.D.; Dwelley, P.C. Mineralized Veins and Breccias of the Cripple Creek District, Colorado. *Econ. Geol.* **1985**, *80*, 1669–1688. [[CrossRef](#)]
10. Pass, H.E. Breccia-Hosted Chemical and Mineralogical Zonation Patterns of the Northeast Zone, Mt. Polley Cu-Ag-Au Alkalic Porphyry Deposit, British Columbia, Canada. Ph.D. Thesis, University of Tasmania, Hobart, Australia, 2010.
11. Davies, A.G.S. Geology and Genesis of the Kelian Gold Deposit, East Kalimantan, Indonesia. Ph.D. Thesis, University of Tasmania, Hobart, Australia, 2002.
12. Blackwell, J.L. Characteristics and Origins of Breccias in a Volcanic Hosted Alkalic Epithermal Gold Deposit, Ladolam, Lihir Island, Papua New Guinea. Ph.D. Thesis, University of Tasmania, Hobart, Australia, 2010.
13. Sillitoe, R.H. Intrusion-Related Gold Deposits. In *Gold Metallogeny and Exploration*; Springer: Dordrecht, The Netherlands, 1991; pp. 165–209.
14. Jing, S.-H. *Study of the Geology and Mineralization Rules of the Yixingzhai Gold Deposit, Fanshi County, Shanxi Province*; Unpublished Geological Report; 211 Geological Team of Shanxi Bureau of Geology and Mineral Resources: Taiyuan, China, 1985.
15. Li, S.; Ma, X. Crypto Explosive Rock and Its Ore-Forming Sense to Gold-Silver Deposit in the Northeastern Shanxi Province, China. *Contrib. Geol. Miner. Resour. Res.* **1999**, *14*, 8–14.

16. Zhang, J.-Q.; Li, S.-R.; Santosh, M.; Li, Q.; Niu, S.-D.; Lu, J.; Yan, L.-N. The Diaquan Ag-Cu Polymetallic Skarn Mineralization in Central North China Craton: Timing, Source and Genetic Model. *Ore Geol. Rev.* **2019**, *104*, 745–764. [[CrossRef](#)]
17. Zhang, J.-Q.; Li, S.-R.; Santosh, M.; Niu, S.-D.; Li, Q.; Lu, J. The Magmatic–Hydrothermal Mineralization Systems of the Yixingzhai and Xinzhuang Gold Deposits in the Central North China Craton. *Ore Geol. Rev.* **2017**, *88*, 416–435. [[CrossRef](#)]
18. Zhang, J.-Q.; Li, S.-R.; Santosh, M.; Li, Q.; Niu, S.-D.; Li, Z.-D.; Zhang, X.-G.; Jia, L.-B. Timing and Origin of Mesozoic Magmatism and Metallogeny in the Wutai-Hengshan Region: Implications for Destruction of the North China Craton. *J. Asian Earth Sci.* **2015**, *113*, 677–694. [[CrossRef](#)]
19. Liu, T.; Xiong, S.-F.; Jiang, S.-Y.; Li, H.-L.; Chen, Q.-Z.; Jiang, H. Genesis of the Zhijiadi Ag-Pb-Zn Deposit, Central North China Craton: Constraints from Fluid Inclusions and Stable Isotope Data. *Geofluids* **2017**, *2017*, 4153618. [[CrossRef](#)]
20. Zhang, L.-Z. Element Geochemistry and Age of the Altered-Porphyry Gold Mineralization in Yixingzhai Gold Deposit, Fanshi City, Shanxi Province. *Geol. Miner. Resour. South China* **2018**, *34*, 134–141. [[CrossRef](#)]
21. Zhang, L.-Z.; Chen, L.; Wang, G.; Deng, X.-D.; Li, J.-W. Garnet U-Pb Dating Constraints on the Timing of Breccia Pipes Formation and Genesis of Gold Mineralization in Yixingzhai Gold Deposit, Shanxi Province. *Eart. Sci.* **2020**, *45*, 108. [[CrossRef](#)]
22. Zhang, J.-Q.; Li, S.-R.; Santosh, M.; Luo, J.-Y.; Li, C.-L.; Song, J.-Y.; Lu, J.; Liang, X. The Genesis and Gold Mineralization of the Crypto-Explosive Breccia Pipe in the Yixingzhai Gold Region, Central North China Craton. *Geol. J.* **2020**, *55*, 5664–5680. [[CrossRef](#)]
23. Shao, Y.; Zhang, Y.; Zhang, J.; Ding, Z.; Chen, X.; Liu, Z. Formation Mechanism of Breccia Pipe Type in Yixingzhai Gold Deposit. *J. Cent. South Univ. Technol.* **2008**, *15*, 89–94. [[CrossRef](#)]
24. Zhao, G.; Sun, M.; Wilde, S.A.; Sanzhong, L. Late Archean to Paleoproterozoic Evolution of the North China Craton: Key Issues Revisited. *Precambrian Res.* **2005**, *136*, 177–202. [[CrossRef](#)]
25. Tang, L.; Santosh, M. Neoproterozoic Terrane Assembly and Wilson Cycle in the North China Craton: An Overview from the Central Segment of the Trans-North China Orogen. *Earth-Sci. Rev.* **2018**, *182*, 1–27. [[CrossRef](#)]
26. Tian, Y.Q.; Yu, K.R.; Wang, A.J.; Xu, W.L. Geodynamic of Veined Gold Deposit Mineralization of Wutaishan-Hengshan Area. *J. Geol. Miner. Resour. North China* **1998**, *13*, 301–456.
27. Chang, J.; Audétat, A.; Li, J.-W. Tectono-Magmatic Controls on Decratonic Gold Deposits. *Contrib. Mineral. Petrol.* **2021**, *176*, 69. [[CrossRef](#)]
28. Deng, X.-D.; Li, J.-W.; Wen, G. U-Pb Geochronology of Hydrothermal Zircons from the Early Cretaceous Iron Skarn Deposits in the Handan-Xingtai District, North China Craton. *Econ. Geol.* **2015**, *110*, 2159–2180. [[CrossRef](#)]
29. Chang, Z.-G.; Dong, G.-C.; Somarin, A.K. U-Pb Dating and Trace Element Composition of Zircons from the Gujiao Ore-Bearing Intrusion, Shanxi, China: Implications for Timing and Mineralization of the Guojialiang Iron Skarn Deposit. *Minerals* **2020**, *10*, 316. [[CrossRef](#)]
30. Li, S.-R.; Santosh, M.; Zhang, H.-F.; Luo, J.-Y.; Zhang, J.-Q.; Li, C.-L.; Song, J.-Y.; Zhang, X.-B. Metallogeny in Response to Lithospheric Thinning and Craton Destruction: Geochemistry and U–Pb Zircon Chronology of the Yixingzhai Gold Deposit, Central North China Craton. *Ore Geol. Rev.* **2014**, *56*, 457–471. [[CrossRef](#)]
31. Deng, X.-R.; Deng, X.-D.; Zhang, L.-Z.; Gao, W.-S.; Li, Y.-X.; Yang, H.-P.; Li, Z.-B. U-Pb Geochronology and Trace Element Analysis of Titanite from the Diaquan Porphyry-Skarn Polymetallic Deposit, North China: Implication for Cu-Ag-Mo Mineralization. *Earth Sci.* **2023**, *48*, 3327–3341. [[CrossRef](#)]
32. Li, J.; Li, N.; Wang, M.; Song, Y.; Tang, Z.; Zhang, P.; Wang, G.; Zhang, L. Formation of the Miaoan Au-Polymetallic Deposit in the Northern Taihang Mountain, North China Craton: Ore Geology, Geochronological and Geochemical Perspectives. *Minerals* **2022**, *12*, 1144. [[CrossRef](#)]
33. Wang, S. Age Determinations of  $^{40}\text{Ar}$ - $^{40}\text{K}$ ,  $^{40}\text{Ar}$ - $^{39}\text{Ar}$  and Radiogenic  $^{40}\text{Ar}$  Released Characteristics on K-Ar Geostandards of China. *Chin. J. Geol.* **1983**, *18*, 315–323.
34. Bai, X.-J.; Qiu, H.-N.; Liu, W.-G.; Mei, L.-F. Automatic  $^{40}\text{Ar}/^{39}\text{Ar}$  Dating Techniques Using Multicollector ARGUS VI Noble Gas Mass Spectrometer with Self-Made Peripheral Apparatus. *J. Earth Sci.* **2018**, *29*, 408–415. [[CrossRef](#)]
35. Koppers, A.A.P. ArArCALC—Software for  $^{40}\text{Ar}/^{39}\text{Ar}$  Age Calculations. *Comput. Geosci.* **2002**, *28*, 605–619. [[CrossRef](#)]
36. Steiger, R.H.; Jäger, E. Subcommittee on Geochronology: Convention on the Use of Decay Constants in Geo- and Cosmochronology. *Earth Planet. Sci. Lett.* **1977**, *36*, 359–362. [[CrossRef](#)]
37. Fu, J.; Hu, Z.; Li, J.; Yang, L.; Zhang, W.; Liu, Y.; Li, Q.; Zong, K.; Hu, S. Accurate Determination of Sulfur Isotopes ( $\delta^{33}\text{S}$  and  $\delta^{34}\text{S}$ ) in Sulfides and Elemental Sulfur by Femtosecond Laser Ablation MC-ICP-MS with Non-Matrix Matched Calibration. *J. Anal. At. Spectrom.* **2017**, *32*, 2341–2351. [[CrossRef](#)]
38. Li, R.; Xia, X.; Yang, S.; Chen, H.; Yang, Q. Off-Mount Calibration and One New Potential Pyrrhotite Reference Material for Sulfur Isotope Measurement by Secondary Ion Mass Spectrometry. *Geostand. Geoanal. Res.* **2019**, *43*, 177–187. [[CrossRef](#)]
39. Zhang, W.; Hu, Z.; Liu, Y. Iso-Compass: New Freeware Software for Isotopic Data Reduction of LA-MC-ICP-MS. *J. Anal. At. Spectrom.* **2020**, *35*, 1087–1096. [[CrossRef](#)]
40. Turner, G.; Cadogan, P.H. Possible Effects of  $^{39}\text{Ar}$  Recoil in  $^{40}\text{Ar}$ - $^{39}\text{Ar}$  Dating. In Proceedings of the Fifth Lunar Science Conference, Houston, TX, USA, 18–22 March 1974; Volume 2, pp. 1601–1615.
41. Hoefs, J. *Stable Isotope Geochemistry*; Springer Textbooks in Earth Sciences, Geography and Environment; Springer International Publishing: Cham, Switzerland, 2021; ISBN 978-3-030-77691-6.
42. Luo, G.; Ono, S.; Huang, J.; Algeo, T.J.; Li, C.; Zhou, L.; Robinson, A.; Lyons, T.W.; Xie, S. Decline in Oceanic Sulfate Levels during the Early Mesoproterozoic. *Precambrian Res.* **2015**, *258*, 36–47. [[CrossRef](#)]

43. Meinert, L.D.; Dipple, G.M.; Nicolescu, S. World Skarn Deposits. In *One Hundredth Anniversary Volume*; Society of Economic Geologists: Littleton, CO, USA, 2005; ISBN 978-1-887483-01-8.
44. Dong, G.; Morrison, G.W. Adularia in Epithermal Veins, Queensland: Morphology, Structural State and Origin. *Miner. Depos.* **1995**, *30*, 11–19. [[CrossRef](#)]
45. Chiaradia, M.; Schaltegger, U.; Spikings, R.; Wotzlaw, J.-F.; Ovtcharova, M. How Accurately Can We Date the Duration of Magmatic-Hydrothermal Events in Porphyry Systems?—An Invited Paper. *Econ. Geol.* **2013**, *108*, 565–584. [[CrossRef](#)]
46. Horstwood, M.S.A.; Košler, J.; Gehrels, G.; Jackson, S.E.; McLean, N.M.; Paton, C.; Pearson, N.J.; Sircombe, K.; Sylvester, P.; Vermeesch, P.; et al. Community-Derived Standards for LA-ICP-MS U-(Th)Pb Geochronology—Uncertainty Propagation, Age Interpretation and Data Reporting. *Geostand. Geoanal. Res.* **2016**, *40*, 311–332. [[CrossRef](#)]
47. Chelle-Michou, C.; Schaltegger, U. U-Pb Dating of Mineral Deposits: From Age Constraints to Ore-Forming Processes. In *Isotopes in Economic Geology, Metallogenesis and Exploration*; Huston, D., Gutzmer, J., Eds.; Mineral Resource Reviews; Springer International Publishing: Cham, Switzerland, 2023; pp. 37–87. ISBN 978-3-031-27896-9.
48. Ohmoto, H. Systematics of Sulfur and Carbon Isotopes in Hydrothermal Ore Deposits. *Econ. Geol.* **1972**, *67*, 551–578. [[CrossRef](#)]
49. Zhu, R.; Fan, H.; Li, J.; Meng, Q.; Li, S.; Zeng, Q. Decratonic Gold Deposits. *Sci. China Earth Sci.* **2015**, *58*, 1523–1537. [[CrossRef](#)]
50. Phillips, G.N.; Evans, K.A. Role of CO<sub>2</sub> in the Formation of Gold Deposits. *Nature* **2004**, *429*, 860–863. [[CrossRef](#)]
51. Ohmoto, H.; Rye, R.O.; Barnes, H.L. *Geochemistry of Hydrothermal Ore Deposits*; John Willey & Sons Inc.: Hoboken, NJ, USA, 1979; Volume 517, p. 612.
52. Hutchison, W.; Finch, A.A.; Boyce, A.J. The Sulfur Isotope Evolution of Magmatic-Hydrothermal Fluids: Insights into Ore-Forming Processes. *Geochim. Cosmochim. Acta* **2020**, *288*, 176–198. [[CrossRef](#)]

**Disclaimer/Publisher’s Note:** The statements, opinions and data contained in all publications are solely those of the individual author(s) and contributor(s) and not of MDPI and/or the editor(s). MDPI and/or the editor(s) disclaim responsibility for any injury to people or property resulting from any ideas, methods, instructions or products referred to in the content.